

Prelaunch characterization of the Ozone Monitoring Instrument transfer function in the spectral domain

Ruud Dirksen, Marcel Dobber, Robert Voors, and Pieter Levelt

A method and an experimental measurement setup to accurately characterize the instrument transfer function in the spectral domain for hyperspectral spectrometers in the ultraviolet–visible wavelength range are described. The application to the on-ground calibration of the Ozone Monitoring Instrument (OMI) on board the Earth Observing System Aura satellite is presented and discussed. With this method and setup, based on an echelle grating, a sampling of the instrument transfer function in the spectral domain can be selected and is not limited by the spectral resolution and sampling of the spectrometer that is being characterized. The importance of accurately knowing the OMI instrument transfer functions in the spectral domain for in-flight differential optical absorption spectroscopy retrievals and wavelength calibration is discussed. The analysis of the OMI measurement data is presented and shows that the instrument transfer functions in the spectral domain as a function of wavelength and viewing angle can be determined with high accuracy. © 2006 Optical Society of America

OCIS codes: 000.2170, 080.2740, 120.4640, 230.1950, 280.1310, 300.6190.

1. Introduction

The Ozone Monitoring Instrument (OMI) was launched on board the Earth Observing System (EOS) Aura satellite on 15 July 2004. The OMI is a hyperspectral instrument that passively probes the backscattered sunlight from the Earth's atmosphere in nadir in the spectral range of 270–500 nm. The instrument is equipped with two two-dimensional CCD detectors that allow us to obtain daily global coverage at the equator with high spatial resolution. The telescope is designed to provide a cross-track field of view of 115°. The mission objectives of the OMI concern the recovery of the ozone layer, the depletion of ozone at the poles, tropospheric air pollution, and climate change. The Earth atmospheric retrieval techniques applied to OMI measurement data include algorithms developed for the NASA Total Ozone Mapping Spectrometer (TOMS) instrument¹ and differential optical absorption spectro-

scopy^{2–4} (DOAS) algorithms developed for the OMI at the Royal Netherlands Meteorological Institute (KNMI).

Total column measurements of ozone, nitrogen dioxide, and other trace gases are routinely made. The vertical distribution of ozone is determined by a method that makes use of the rapid increase in the ozone absorption cross section toward shorter wavelengths (Hartley bands).^{5,6} The OMI follows in the footsteps of predecessor instruments such as the Global Ozone Monitoring Experiment (GOME), the Scanning Imaging Absorption Spectrometer for Atmospheric Cartography (SCIAMACHY), the TOMS, and the Solar Backscatter Ultraviolet (SBUV) instrument.

For the OMI various of the Earth's atmospheric constituents and trace gases are retrieved using DOAS,^{2–4} for which an accurate characterization of the spectral instrument transfer function is essential. These gases include ozone (331.6–336.6 nm), nitrogen dioxide (405–465 nm), formaldehyde (324–357 nm), BrO (323–347 nm), and OCIO (363–402 nm). The retrieval techniques for these constituents are based on comparing the measured Sun-normalized Earth radiances (also called Earth reflectances) to high-resolution absorption cross-section spectra from the literature convolved with the OMI instrument transfer function (ITF) in the spectral domain. The absorption cross-section data from the literature have been obtained with dedicated experimental equipment un-

R. Dirksen is with the Royal Netherlands Meteorological Institute, P.O. Box 201, 3730 AE De Bilt, The Netherlands and the Space Research Organization Netherlands, Sorbonnelaan 2, 3584 CA Utrecht, The Netherlands. M. Dobber (dobber@knmi.nl), R. Voors, and P. Levelt are with the Royal Netherlands Meteorological Institute, P.O. Box 201, 3730 AE De Bilt, The Netherlands.

Received 23 August 2005; revised 22 November 2005; accepted 25 November 2005; posted 1 December 2005 (Doc. ID 64313).

0003-6935/06/173972-10\$15.00/0

© 2006 Optical Society of America

der closely monitored experimental conditions (i.e., temperature and pressure). Early in the OMI project the choice was made to follow this approach for DOAS-type retrievals. In an earlier publication the validity of the retrieval approach was discussed and demonstrated.⁷ The alternative approach of using reference absorption spectra obtained with the instrument itself at various temperatures and pressures is not employed in the OMI project.

An accurate characterization of the ITF in the spectral domain is essential for the retrieval of the Earth's atmospheric constituents from the OMI measurement data. The ITF in the spectral domain is the instrument response to a monochromatic input signal. It is the monochromatic image of the entrance slit of the spectrometer on the CCD detector convolved with the response function of the detector. Furthermore, the OMI in-flight spectral calibration is done with the solar Fraunhofer lines (both Earth and Sun spectra) and atmospheric absorption lines (Earth spectra). The measured spectra are spectrally compared to a high-resolution solar spectrum and to trace gas absorption spectra from the literature convolved with the ITFs. Hence an accurate characterization of the ITF is also important for accurate in-flight spectral calibration of the measured Earth and Sun spectra. For the OMI the ITF depends on wavelength (the column or horizontal dimension on the CCD detectors) and viewing direction (the row or vertical dimension on the CCD detectors). Both dependencies must be characterized accurately. It is also important, given the applications for the OMI, to know the ITF accurately up to wavelengths 3σ from the wavelength corresponding to the maximum of the ITF, where the instrument response typically becomes lower than 1% of the maximum. In this paper σ is the FWHM, or simply the width, of the profile. Given the above applications in the OMI project, the required scientific accuracy for the ITF has been set to 2% within $\pm 2\sigma$ of the ITF maximum and 10% between $\pm 2\sigma$ and $\pm 3\sigma$. This is the accuracy with which the ITF needs to be characterized.

For the OMI a dedicated method and an experimental setup based on an echelle grating were developed to characterize the ITF accurately as a function of wavelength and viewing direction on the ground. This is the subject of this paper. The OMI optical design will be described briefly in Section 2. Subsequently, the experimental setup for characterizing the ITF and the analysis of the measurement data will be described. It will be shown that with this equipment and these analysis methods the ITF in the spectral domain can be characterized with the required high accuracy.

2. Ozone Monitoring Instrument

The OMI is equipped with a telescope system that enables the observation of the Earth at an altitude of approximately 700 km with an instantaneous cross-track field of view of 115° with daily global coverage at the equator. The telescope, consisting of

a primary convex telescope mirror, a polarization scrambler, and a secondary convex telescope mirror, images the Earth's light onto the spectrometer's entrance slit (44 mm long, 0.3 mm wide). The instrument has separate UV and visible (VIS) optical channels each equipped with a $780 \text{ pixel} \times 576 \text{ pixel}$ CCD detector that is operated in binned mode with a binning factor of 8 (global mode) to provide spectra of 780 pixels in the spectral dimension and 60 pixels in the viewing direction dimension. The resulting ground pixel sizes per channel are listed in Table 1, along with a number of other OMI parameters. The UV channel is optically divided into a wavelength range below 311 nm (UV1) and one

Table 1. OMI Properties

Property	Value
Spectral range	UV1: 264–311 nm UV2: 307–383 nm VIS: 349–504 nm
Spectral sampling	UV1: 0.33 nm/px UV2: 0.14 nm/px VIS: 0.21 nm/px
Spectral resolution (FWHM)	UV1: 1.9 px = 0.63 nm UV2: 3.0 px = 0.42 nm VIS: 3.0 px = 0.63 nm
Telescope cross-track swath field of view	115° (2600 km on the ground)
Telescope along-track flight instantaneous field of view	1.0° (13 km on the ground)
Ground pixel size at nadir, global mode (electronic binning factor 8)	UV1: 13 km \times 48 km, 30 binned pixels UV2: 13 km \times 24 km, 60 binned pixels VIS: 13 km \times 24 km, 60 binned pixels
Silicon CCD detectors	780×576 (spectral \times spatial) pixels
Operational CCD temperature	UV: 265.07 K VIS: 264.99 K
In-orbit CCD temperature excursion	UV and VIS: ± 10 mK (stabilized)
Operational optical bench temperature	264 K
In-orbit optical bench temperature excursion	± 300 mK
Duty cycle	60 min on daylight side (Earth and Sun measurements) 10–30 min on eclipse side (calibration measurements)
Average data rate	0.8 Mbits/s
Power	66 W
Mass	65 kg
Size	50 cm \times 40 cm \times 35 cm
Orbit	Polar, Sun-synchronous Average altitude: 705 km (438 mi) Orbit period: 98 min, 53 s Ascending node local time: 1:42 PM

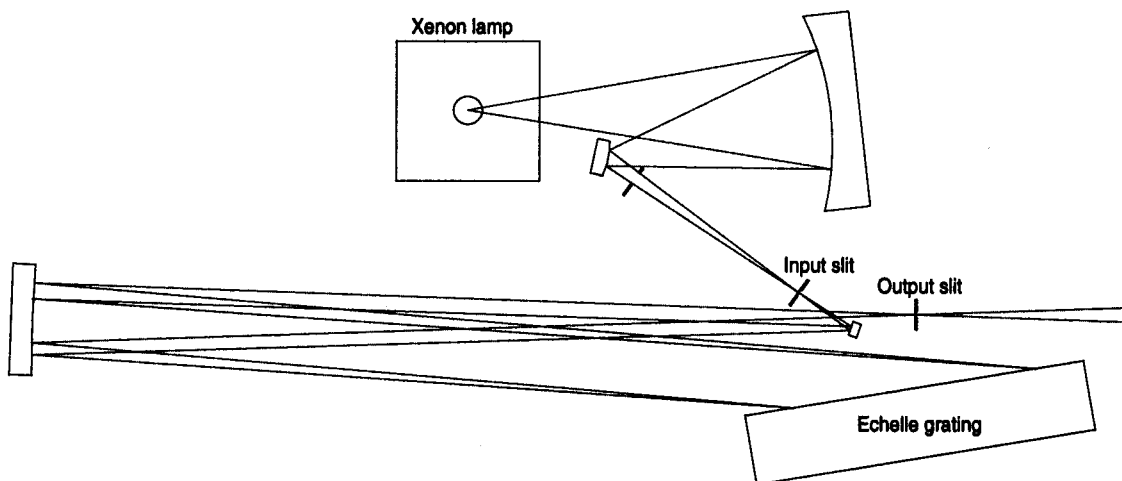


Fig. 1. Schematic optical layout of the echelle-grating optical stimulus to characterize the instrument transfer function in the spectral domain.

above 307 nm (UV2), which are imaged on different regions of the same CCD detector. This has been done to suppress spectral stray light and to optimize the instrument's optical and electronic settings for the wavelength range below 311 nm separately, because in that wavelength range the Earth's fluxes decrease by three to four orders of magnitude as a result of absorption by ozone in the Hartley–Huggins bands. In addition to an optical path with a view of the Earth, the OMI also has a separate Sun measurement port that can be closed when not looking at the Sun. Sunlight illuminates one of three reflectance diffusers that are mounted on a carousel mechanism. A folding mirror located on another mechanism reflects the sunlight to the polarization scrambler and the remainder of the optical system while blocking the Earth's light. The remainder of the optical system, including the secondary telescope mirror and the entrance slit of the spectrometer, is exactly the same for the Sun and Earth viewing modes. The OMI is also equipped with a white-light source that illuminates the entire entrance slit by means of a transmission diffuser. The white-light source is used mainly for detector calibration purposes. For on-ground measurements there was also a possibility of illuminating the transmission diffuser by means of the white-light-source path using external light sources. This optical path is called the calibration port. The Sun port, the white-light-source port, and the calibration port have in common that they can all illuminate the entire entrance slit of the spectrometer with more or less parallel beams. To achieve this in the Earth mode the complete 115° field of view needs to be illuminated. The calibration port of the OMI was used on the ground for the ITF characterization measurements described in this paper. In this way all viewing directions could be investigated simultaneously. Further details on the optical and electronic design of the OMI can be found in Refs. 8–15.

3. Instrument Transfer Function Characterization Measurements and Results

A. Echelle-Grating Instrument Transfer Function Characterization Setup and Measurements

The optical configuration of the echelle ITF characterization optical stimulus is schematically shown in Fig. 1.¹⁶ A 150 W high-pressure xenon arc discharge lamp is imaged by a Schwarzschild mirror configuration on the entrance slit of an echelle monochromator. The light passing through the input slit is imaged as a parallel beam on the echelle grating by the concave mirror to the left in Fig. 1. The echelle grating is illuminated at grazing incidence, and the diffracted beam travels back almost in the same direction as the initial white-light beam. The output slit transmits only a small part of the echelle spectrum. A system of two convex lenses, not shown in Fig. 1, parallelizes the beam toward the OMI, which is located in the thermal-vacuum chamber at flight-representative temperature (optical bench, 264 K; detectors, 265 K) and pressure ($<10^{-5}$ mbar) environmental conditions. The echelle optical stimulus beam with a diameter of approximately 50 mm illuminated the OMI calibration port homogeneously, which enables accurate ITF characterization measurements of all pertinent viewing angles simultaneously.

It is of crucial importance for accurate characterization of the ITF in the spectral domain that the 0.3 mm width of the OMI entrance slit be illuminated homogeneously or unrepresentative ITFs will be obtained. The exit beam of the echelle-grating optical stimulus is sufficiently spatially uniform for all wavelengths in the range of 270–500 nm. The transmission diffuser inside the OMI in the calibration port optical path improves this uniformity further, thus ensuring that the width of the OMI entrance slit is illuminated homogeneously.

The echelle grating, which is made from zerodur with an aluminum coating, is the most critical com-

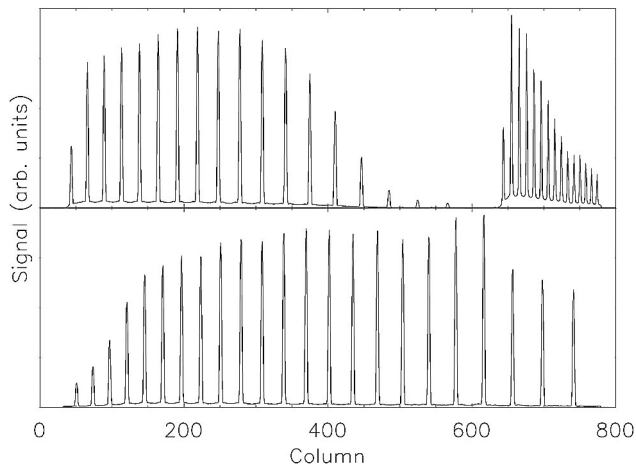


Fig. 2. Echelle spectrum measured by the OMI: top panel, UV1 channel (right) and UV2 channel (left); lower panel, VIS channel. The column dimension is the spectral dimension. The stimulus stray light shows up as a background, most notably in the UV1 channel (columns 600–800 in the UV channel).

ponent of the experimental setup. The grating surface is 50 mm × 220 mm and the blaze angle is 76°. The grating is ruled with 72 lines/mm, resulting in a grating constant d of 1.39×10^{-5} m. The incidence angle and the angle of diffraction on the grating are approximately 74.5° and 75.5°, respectively. The wavelengths of the grating orders in the exit beam can be calculated from the grating equation

$$d(\sin \theta_i + \sin \theta_d) = m\lambda, \quad (1)$$

where d is the grating constant of 1.39×10^{-5} m, λ is the air wavelength, θ_i is the angle of incidence of approximately 74.5°, θ_d is the angle of diffraction of approximately 75.5°, and m is the grating diffraction order. These echelle-grating properties result in an exit beam that contains many spectrally narrow orders: in the OMI UV1 channel approximately 15 orders (from $m = 87$ to 101 at an incidence angle of approximately 74.5°), in the UV2 channel approximately 18 orders (from $m = 70$ to 87 at an incidence angle of approximately 74.5°), and in the VIS channel approximately 23 orders (from $m = 54$ to 76 at an incidence angle of approximately 74.5°). An example of a measured spectrum is shown in Fig. 2 for the central nadir row. The peak separation between adjacent orders is smaller for lower wavelengths in the UV1 channel (approximately 2.7 nm at 266 nm between $m = 100$ and 101) and larger for higher wavelengths in the VIS channel (approximately 9.0 nm at 496 nm between $m = 54$ and 55).

The entrance and exit slits of the echelle-grating optical stimulus can be chosen from three sets: nominal resolution (0.5 mm × 8.0 mm), medium resolution (1.0 mm × 8.0 mm), or low resolution (2.0 mm × 8.0 mm). The entrance and exit slits are the same size. In these ranges of slit widths the spectral widths of the output grating orders scale linearly with the widths of the slits, whereas the output flux scales

Table 2. Calculated Spectral Resolution for Various Grating Orders^a

Echelle-Grating Order m	λ_{air} (nm)	$\Delta\lambda$ (nm), FWHM
54	496.9	0.053
55	487.9	0.051
60	447.2	0.047
65	412.8	0.043
70	383.3	0.041
75	357.8	0.038
80	335.4	0.036
85	315.7	0.033
90	298.1	0.031
95	282.5	0.030
99	271.0	0.028
100	268.3	0.028

^aThe grating orders are given for a nominal slit width of 0.5 mm. The value of $\Delta\lambda$ is the FWHM of the spectral grating order peaks in the exit beam.

quadratically with the widths of the slits. For the OMI measurements slits with a width of 0.5 mm were used. For these slits the FWHM $\Delta\lambda$ of the spectral grating orders in the exit beam was calculated. The results are shown in Table 2. Over the spectral range of the OMI, $\Delta\lambda$ varies from 0.028 nm at 270 nm to 0.053 nm at 500 nm, which is at least an order of magnitude lower than the spectral resolution of the OMI at these wavelengths (see Table 1). This is an important prerequisite for accurate ITF characterization measurements, because otherwise the width of the grating order lines cannot be neglected in the ITF measurement analysis.

The echelle grating is located on a computer-controlled rotational stage, which enables accurate and reproducible angle movement of the grating. During the OMI measurements an angular step size of 0.02° was employed, corresponding to a wavelength shift of approximately 0.04 nm for an order near 490 nm. This feature of the echelle-grating ITF characterization optical stimulus is one of the more essential ones. An echelle stimulus spectrum at a fixed grating position as measured by the OMI shows ITF profiles of all grating orders present in the stimulus exit beam with at most five measurement points (CCD pixels) per line at the viewing direction under consideration, as shown in the top panel of Fig. 3. However, if we focus on the response of a single CCD detector pixel as a function of an echelle-grating rotation angle, the number of sampling points in the measured ITF is determined by the step size of the grating rotation, as shown in the lower panel of Fig. 3, rather than by the spectral sampling and resolution of the OMI, as would be the case for conventional methods of determining the ITF. This measurement principle enables a characterization of the ITF using typically ten times more sampling points to fit the ITF response shape accurately. For the OMI measurements the echelle grating was scanned over a 5° angular range centered around the blaze angle of 76°. At the blaze angle the reflection

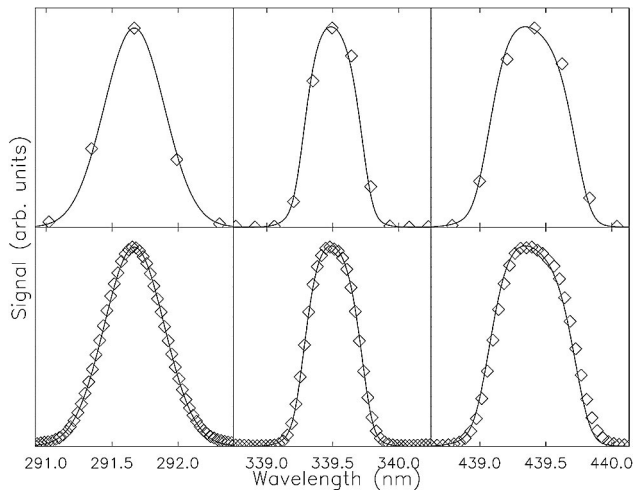


Fig. 3. The ITF of the OMI in the spectral domain is typically sampled by 4–5 detector pixels. By using the dedicated echelle-grating ITF characterization optical stimulus a sampling of the ITF that is ten times higher is obtained. The plots to the left compare a spectral peak registered by the OMI CCD in the UV1 channel (upper plot) to the same peak sampled using the ITF characterization optical stimulus (lower plot). The same for the UV2 (middle) and VIS channels (right).

efficiency of the grating is maximal, so, by scanning around this angle, the highest stimulus output is obtained. With the 5° scanning range every detector pixel sees the complete passage of at least one grating order. The measurements were performed with the OMI in a thermal-vacuum chamber at flight-representative thermal-vacuum conditions (with an optical bench temperature of 264 K). This is important, because the ITFs are expected to change with the temperature of the optical bench. By illuminating the instrument by means of the calibration port transmission diffuser, all CCD rows are illuminated instantaneously. The ITFs for all viewing directions and wavelengths are measured in one measurement run, which takes approximately 24 h. It is important to correct for the echelle-grating efficiency variation as a function of rotation angle and for the stray light originating from the grating in the optical stimulus. Both corrections are discussed in detail in the Sub-section 3.B.

The echelle-grating ITF characterization optical stimulus has also been used to derive the on-ground spectral calibration of the OMI. Whereas accurate knowledge of the wavelengths of the grating order peaks is not important for characterization of the ITFs, it is important for performing the wavelength calibration of the OMI. The actual optical stimulus parameters are known with insufficient accuracy for this purpose, and for this reason the stimulus has to be commissioned with respect to external sources. The OMI wavelength calibration is described by polynomial expressions in the column dimension (wavelength dimension) for each row (viewing direction) and for each optical channel (UV1, UV2, and VIS). By using the echelle-grating optical stimulus all poly-

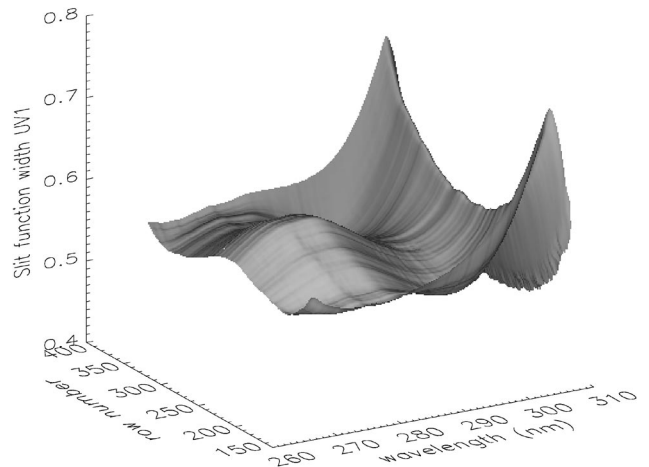


Fig. 4. Width of the ITF in the spectral domain as a function of wavelength and row number for the UV1 channel.

mial coefficients but the zero-order term (independent of column) can be calibrated accurately. The zero-order coefficient was determined by comparing the echelle stimulus measurements to measurements with a hollow-cathode low-pressure PtCrNeAr discharge lamp, for which the emission line wavelengths are known with high accuracy. This enabled a pre-launch wavelength calibration to an accuracy of about 0.1 pixel, which is the requirement for pre-launch spectral calibration accuracy. The in-flight wavelength scale is obtained by fitting the solar Fraunhofer absorption lines and the absorption lines from the Earth's atmospheric constituents and trace gases in the measured spectra to a high resolution solar spectrum¹⁷ and to the absorption cross-section literature reference spectra for the Earth's atmospheric constituents and trace gases until an optimal match is found at all pertinent wavelengths. This calibration, which will not be discussed in further detail here, has an accuracy of about 0.01 pixels,

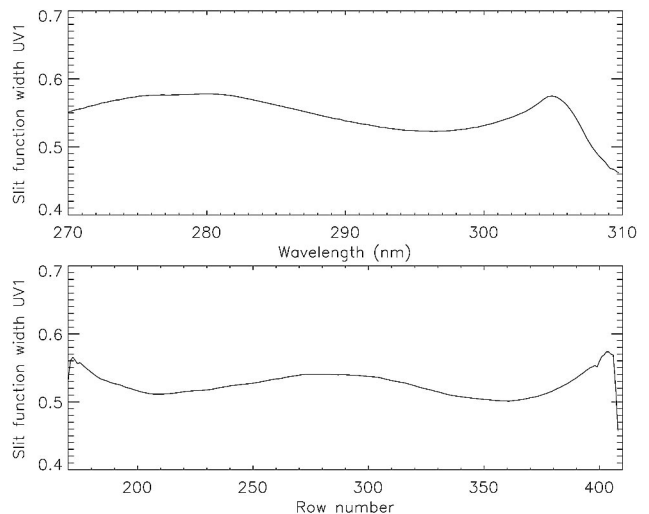


Fig. 5. Cross sections of the spectral width of the ITF as a function of wavelength for row 300 (top panel) and row number for a wavelength of 290 nm (bottom panel) for the UV1 channel.

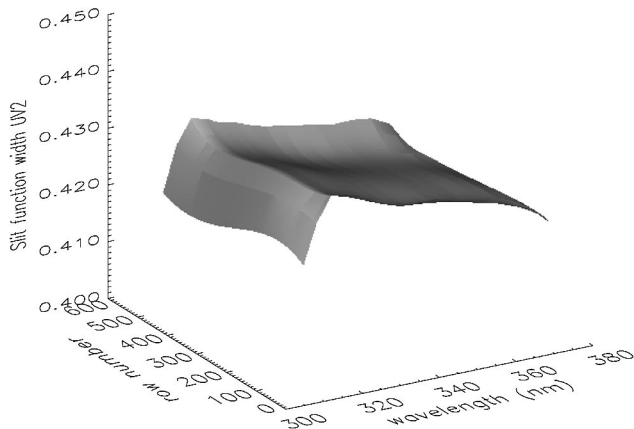


Fig. 6. Spectral width of the ITF as a function of wavelength and row number for the UV2 channel.

which equals the scientific requirement for in-flight spectral calibration accuracy. The in-flight requirement for spectral calibration accuracy is determined by the application of the DOAS retrieval technique to obtain the concentrations of the Earth's various atmospheric constituents and trace gases.

The possibilities of the echelle-grating ITF characterization optical stimulus can be compared to the possibilities of the traditional method of using a hollow-cathode low-pressure discharge lamp (e.g., PtCrNeAr) and to the possibilities of using a wavelength-tunable laser. The echelle-grating optical stimulus has a large number of spectrally narrow (compared to the OMI sampling and resolution) and well-separated lines, whereas the discharge lamp has a large number of narrow lines, which are often blended and not always optimally distributed over the wavelength range. A wavelength-tunable laser emits only one nearly monochromatic spectral line, and to cover a large wavelength range from ultraviolet to visible or even near-infrared, a specialized and complex laser setup is required. Both the echelle grating and laser setups are tunable over very small wavelength changes. This is not the case for the spectral lamp. A laser has significantly higher output flux than the echelle-grating stimulus or the spectral lamp, but the advantage in measurement time is lost by the fact that the laser emits only one line, whereas the other two sources can measure different wavelength regions at the same time. Thus the total measurement time will be comparable. A narrow laser beam will need to be expanded to fill the entrance slit of the instrument homogeneously, which further reduces the flux. A tunable laser is optimally suited for characterizing the ITF outside $2-3\sigma$ from the spectral peak maximum. This is more difficult for the spectral lamp, given the line blending, and for the echelle-grating stimulus, which has to be corrected for the spectral stray light in between the grating order peaks (see Subsection 3.B).

B. Echelle-Grating Instrument Transfer Function Results

During the OMI on-ground calibration-phase ITF measurements, five unbinned CCD images (576

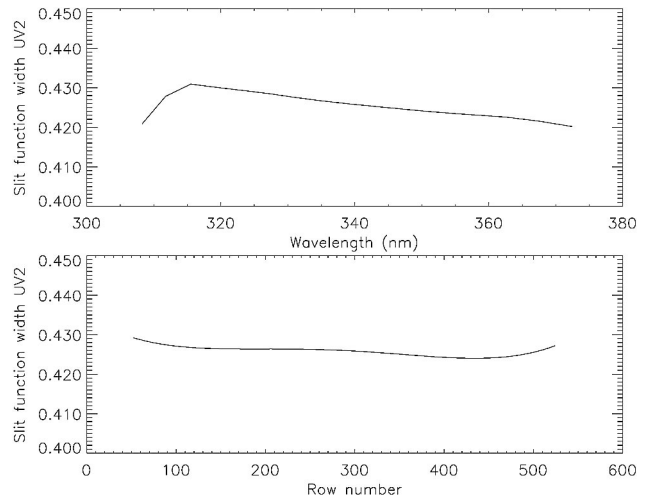


Fig. 7. Cross sections of the spectral width of the ITF as a function of wavelength for row 300 (top panel) and row number for a wavelength of 343 nm (bottom panel) for the UV2 channel.

rows) were recorded for every echelle-grating position. These images were averaged to improve the signal-to-noise ratio (SNR) of the measurements. The CCD dark current signal was corrected for by subtracting a dedicated measurement performed with the stimulus switched off. Furthermore, the measurement data were corrected for all OMI detector and electronic settings. The OMI ITF is determined by measuring the response of a CCD pixel to a passing echelle peak of the optical stimulus. This is measured simultaneously for all CCD pixels, i.e., all wavelengths and viewing angles. The rotation of the grating changes the incidence and diffraction angles on the echelle grating. This changes the wavelengths of the diffraction orders according to Eq. (1). The rotation of the grating also influences the intensity of the peaks in the output beam, as the grating efficiency depends on θ_i and θ_d . As a consequence the measured signal in each CCD pixel consists of the combined effect of the ITF response to a passing echelle peak and the more slowly varying intensity of

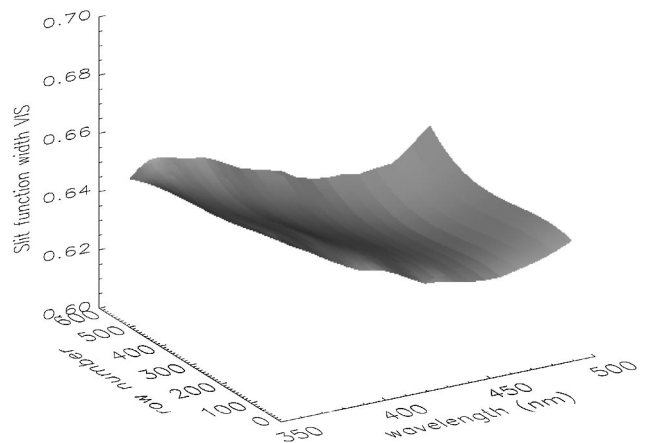


Fig. 8. Spectral width of the ITF as a function of wavelength and row number for the VIS channel.

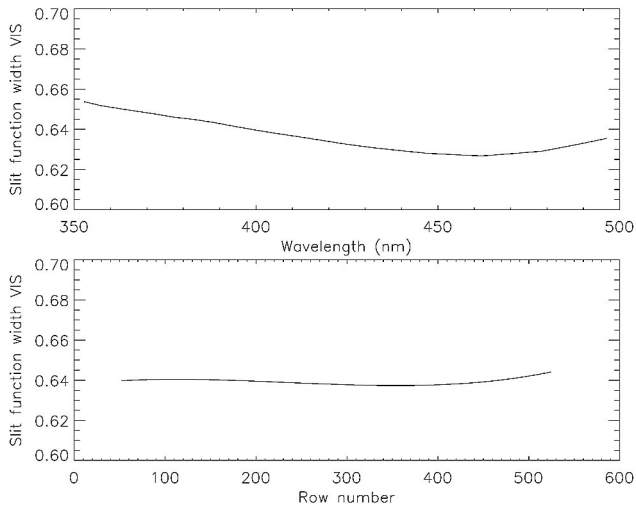


Fig. 9. Cross sections of the spectral width of the ITF as a function of wavelength for row 300 (top panel) and row number for a wavelength of 406 nm (bottom panel) for the VIS channel.

that peak. For an accurate characterization of the ITF there must be a correction for the latter effect. The intensity variations as a function of grating angle have to be corrected for each grating order individually, because the grating efficiency change as a function of illumination geometry is wavelength dependent. The use of a broadband detector to monitor the output of the stimulus for this purpose is not sufficient because this detector records the integrated reflectivity of the grating over all wavelengths rather than the wavelength-dependent intensity as a function of the grating rotation angle. This would make the grating efficiency correction far less accurate and reduce the accuracy of the ITF characterization. The relation between the peak intensities and the grating angles was determined by fitting the position and amplitude of each grating order peak within the OMI wavelength range as it moves over the CCD detector. By using the known radiometric sensitivity of the OMI as a function of wavelength and viewing angle, the relative output flux of each peak in the optical stimulus output beam as a function of the grating position is calibrated. The radiometrically calibrated OMI is thus used to calibrate the wavelength-dependent output flux of the echelle-grating ITF characterization optical stimulus. The stimulus output flux correction is accurate to about 1.5%.

The images recorded by the OMI also need to be corrected for the spectral stray light originating from the echelle optical stimulus itself. This spectral stray light originates mainly from the echelle grating and shows up as a more or less wavelength-independent background, as can be seen in Fig. 2. At low signal levels, i.e., at wavelength separations of more than 3σ from the maximum of the ITF response, it becomes increasingly difficult to distinguish between spectral stray light from the optical stimulus and the wings of the ITF itself. This is a disadvantage of the echelle-grating ITF characterization optical stimulus as compared to a wavelength tunable laser, for example, for

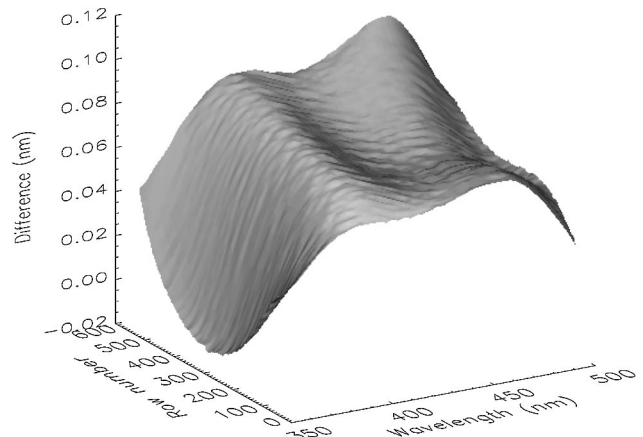


Fig. 10. Surface plot of the asymmetry of the ITF in the spectral domain in the VIS channel. Asymmetry is given as the difference between the wavelength distance λ_p -left 50% point and λ_p -right 50% point, with λ_p being the wavelength of the profile maximum.

which the spectral stray light at wavelengths 3σ from the maximum of the ITF response can be made negligible. For the echelle-grating optical stimulus the spectral stray light was minimized in the design by the use of baffles and the entrance and exit slits, but the stray light cannot be neglected in the data analysis.

Both the spectral distribution and the intensity of the spectral stray light originating from the optical stimulus depend on the echelle-grating position. This necessitates determining the shape of the stray light background for measurements at each grating position before applying the stray light correction. The shape of the stray light background as a function of wavelength is determined by interpolating between the signal levels in between the grating order peaks. The magnitude of the optical stimulus spectral stray light increases from approximately 2% in the VIS channel to approximately 10% in the UV1 channel. Independent spectral stray light measurements on the OMI using different optical stimuli have con-

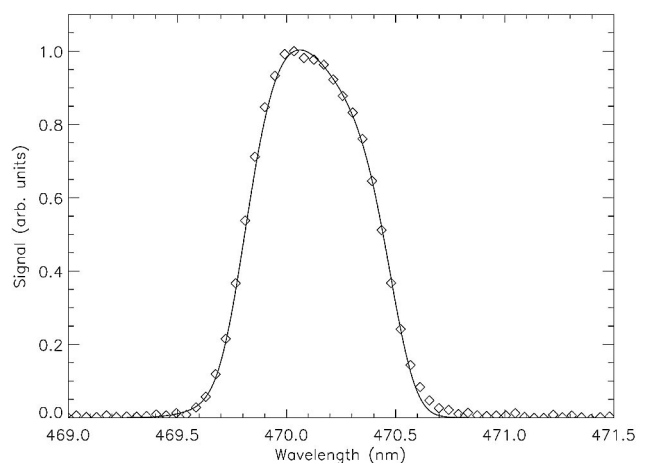


Fig. 11. Example of an asymmetric ITF in the spectral domain in the VIS channel at row 499 and wavelength 470 nm.

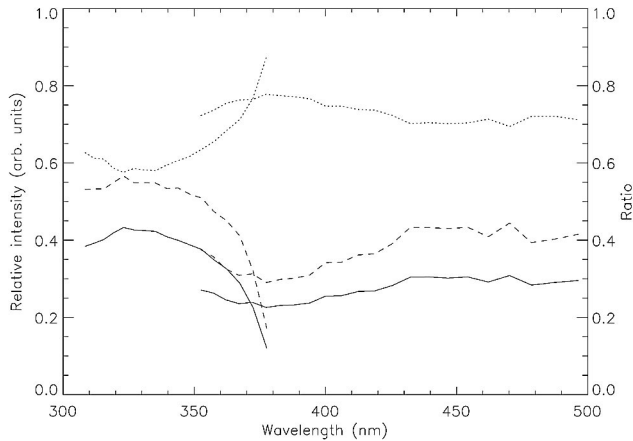


Fig. 12. Wavelength dependence of the ITF parameters A_0 and A_1 for row 300 in the UV2 and VIS channels. Solid curve and left scale, A_0 ; dotted curve and left scale, A_1 ; dashed curve and right scale, A_0/A_1 .

firming that the stray light observed in the echelle-grating optical stimulus measurements originates from the stimulus itself rather than from the OMI for which the spectral stray light is much smaller.⁸ With the method described above the accuracy of the stray light correction from the optical stimulus is approximately 1% within $\pm 2\sigma$ from the maximum of the ITF profile and approximately 10% between $\pm 2\sigma$ and $\pm 3\sigma$, where the useful signals of the ITF profile are much smaller. Given the SNR (uncertainty smaller than 0.5%), reproducibility, and accuracy of the radiometric (1.5%) and stimulus stray light corrections (see above), the accuracy of the measured OMI ITFs as a function of wavelength and viewing angle is (1.9%) within $\pm 2\sigma$ of the profile maximum and approximately 10% between $\pm 2\sigma$ and $\pm 3\sigma$ of the profile maximum, which is within the required numbers of 2% and 10%, respectively. The individual uncertainties are independent of each other.

It was found that the measured ITF profiles can be fitted adequately by the following analytical function:

$$A_0 \exp\left\{-\left[\frac{(x-x_0)^2}{w_0}\right]\right\} + A_1 \exp\left\{-\left[\frac{(x-x_1)^4}{w_1}\right]\right\}, \quad (2)$$

where A_0 represents the amplitude; x_0 is the central position; w_0 is the width of the Gauss term; and A_1 , x_1 , and w_1 represent the same parameters for the second term. This function combines a standard Gauss function and a term that yields a profile that has steeper flanks and a flatter top than the regular Gauss function. This function is well suited to describe symmetrical Gaussian-shaped profiles, as well as broadened and asymmetrical profiles as measured for the OMI ITF. Figure 3 shows that the ITF in the UV1 optical channel can be described adequately by a simple Gaussian, whereas the ITFs in the UV2 and VIS channels are shaped differently, which necessitates the use of both terms in Eq. (2).

The FWHM of the ITF directly relates to the spectral resolution of the OMI and is in the case of the

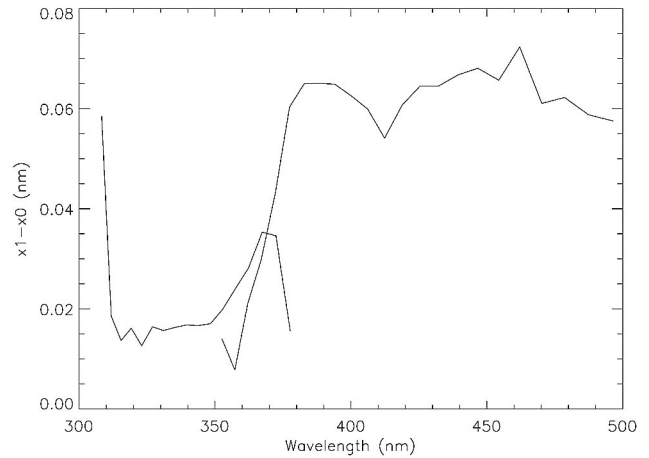


Fig. 13. Wavelength dependence of the difference between ITF parameters x_1 and x_0 for row 300 in the UV2 and VIS channels. This is the difference between the central wavelengths of the Gaussian and the $\exp(-x^4)$ terms in Eq. (2).

UV1 channel calculated directly from the fitted Gauss parameter w_0 . For the UV2 and VIS channels there is no simple analytical expression for the ITF FWHM and it is therefore calculated numerically. The measured and analyzed ITF profiles are fitted for all rows (viewing directions) and for all columns (wavelengths) in all spectral channels with the analytical function described in Eq. (2). The variation of the ITF spectral width as a function of channel, wavelength, and row number (viewing angle) is shown in Figs. 4–9. Figures 4, 6, and 8 show the surface plots of all variables, and Figs. 5, 7, and 9 show the cross-section plots of the ITF spectral width for all three spectral channels. As can be seen from the figures, the ITF width depends on both wavelength and row number. For the UV2 and the VIS channels the width of the ITF varies approximately 5% with wavelength, whereas the variation with row numbers is considerably smaller. In the UV1 channel these variations are

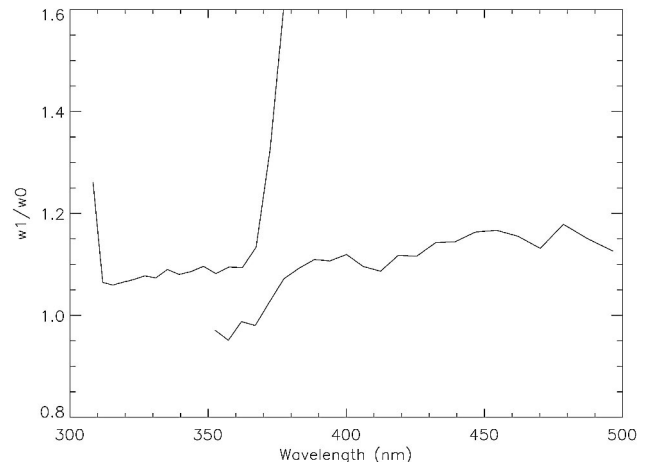


Fig. 14. Wavelength dependence of the ratio of the ITF parameters w_0/w_1 for row 300 in the UV2 and VIS channels. This is the ratio of the width of the Gaussian and the $\exp(-x^4)$ terms in Eq. (2).

larger with up to a 10% variation in width in the row direction and as much as a 20% variation in the spectral direction. Furthermore, a discontinuous behavior of the ITF width is observed at approximately 305 nm. From 295 to 305 nm the width increases with wavelength and then suddenly decreases from 305 to 310 nm. The onset of the observed discontinuous behavior coincides with the beginning of the UV1/UV2 overlap region. This behavior is caused by the segmented mirror that is used to separate the UV1 and UV2 channels in the OMI.⁸ In the UV channel an intermediate spectrum is imaged on a segmented mirror that reflects the part of the spectrum below 310 nm into the UV1 channel and the wavelengths above 310 nm into the UV2 channel. Wavelengths in the overlap region of 305–310 nm end up in both channels, which effectively causes a vignetting of the beam, resulting in a narrower ITF for the wavelengths involved.

Figure 10 illustrates the asymmetry in the VIS channel. The difference in the absolute wavelength differences between the wavelengths at the profile maximum and at half-maximum is shown as a function of wavelength and row number (viewing angle). For nearly all viewing angles and wavelengths the measured ITF is asymmetric, except for the cases where the vertical axis value equals zero. Figure 11 shows the measured and fitted profile at row 499 and wavelength 470 nm in the VIS channel. This profile is asymmetric, in agreement with the results shown in Fig. 10. Figure 12 shows the amplitudes and ratio of the amplitudes of the two terms in Eq. (2) for row 300 in the UV2 and VIS channels. In the UV2 channel the Gaussian-term contribution decreases with increasing wavelength while the contribution of the already dominant second term increases with increasing wavelength. In the VIS channel the second term in Eq. (2) is equally dominant over the first Gaussian term for all wavelengths. Figure 13 shows a similar plot for the wavelength difference $x_1 - x_0$. This plot also shows that the measured ITF profile is asymmetric in the VIS channel and more symmetric in the UV2 channel. Figure 14 shows the ratio of the widths of the two terms in Eq. (2) for row 300 in the UV2 and VIS channels.

4. Conclusions

A measurement method and an echelle-grating-based experimental setup to accurately characterize the wavelength-dependent ITFs in the spectral domain of hyperspectral spectrometers have been presented. The application of this method in the on-ground calibration of the Earth Observing System OMI has been shown. The most important feature of this new method is that the sampling of the measured ITFs in the spectral domain can be chosen from the measurement setup and is not limited by the resolution or sampling rate of the spectrometer that is being characterized. The OMI spectral ITFs in the spectral domain have been characterized with high accuracy and within the requirements as a function of wavelength and viewing angle. The necessary steps to

correct and analyze the data have been described. An accurate knowledge of the OMI ITF in the spectral domain is essential for the Earth's atmospheric constituent retrieval algorithms and for in-flight wavelength calibration.

This research was funded by the Netherlands Agency for Aerospace Programmes (NIVR) within the framework of the Ozone Monitoring Instrument (OMI) project. We thank the Netherlands Organization for Applied Technological Research (TNO) for designing (in particular Huib Visser), building, and commissioning the echelle grating optical stimulus.

References

1. R. D. McPeters, P. K. Bhartia, J. K. Arlin, J. R. Herman, C. G. Wellemeyer, C. J. Seftor, G. Jaross, O. Torres, L. Moy, G. Labow, W. Byerly, S. L. Taylor, T. Swissler, and R. P. Cebula, "1998: Earth probe total ozone mapping spectrometer (TOMS) data products user's guide," NASA Tech. Publ. 1998-1206895.
2. U. Platt, "Differential optical absorption spectroscopy (DOAS)," in *Air Monitoring by Spectroscopic Techniques*, M. W. Sigrist, ed. (Wiley, 1994), pp. 27–84.
3. J. M. C. Plane and N. Smith, "Atmospheric monitoring by differential optical absorption spectroscopy in environmental science," *Advances in Spectroscopy*, R. J. H. Clark and R. E. Hester, eds. (Wiley, 1994), Vol. 24.
4. J. P. Veefkind, J. F. de Haan, E. J. Brinksma, M. Kroon, and P. F. Levelt, "Total ozone from the Ozone Monitoring Instrument (OMI) using the DOAS technique," *IEEE Trans. Geosci. Remote Sens.* **44**, 1239–1244 (2006).
5. F. W. P. Gotz, A. R. Meetham, and G. M. B. Dobson, "The vertical distribution of ozone in the atmosphere," *Proc. R. Soc. London, Ser. A* **145**, 416–446 (1934).
6. C. L. Mateer and J. J. DeLuisi, "A new Umkehr inversion algorithm," *J. Atmos. Terr. Phys.* **54**, 537–556 (1992).
7. M. Dobber, R. Dirksen, R. Voors, G. H. Mount, and P. Levelt, "Ground-based zenith sky abundances and *in situ* gas cross sections for ozone and nitrogen dioxide with the Earth Observing System Aura Ozone Monitoring Instrument," *Appl. Opt.* **44**, 2846–2856 (2005).
8. M. R. Dobber, R. J. Dirksen, P. F. Levelt, G. H. J. van den Oord, R. Voors, Q. Kleipool, G. Jaross, M. Kowalewski, E. Hilsenrath, G. Leppelmeier, J. de Vries, W. Dierssen, and N. Rozemeijer, "Ozone Monitoring Instrument calibration," *IEEE Trans. Geosci. Remote Sens.* **44**, 1209–1238 (2006).
9. P. F. Levelt, E. Hilsenrath, G. W. Leppelmeier, G. H. J. van den Oord, P. K. Bhartia, J. Tamminen, J. F. de Haan, and J. P. Veefkind, "Science objectives of the Ozone Monitoring Instrument," *IEEE Trans. Geosci. Remote Sens.* **44**, 1199–1208 (2006).
10. P. F. Levelt, G. H. J. van den Oord, M. R. Dobber, A. Malkki, H. Visser, J. de Vries, P. Stammes, J. O. V. Lundell, and H. Saari, "The Ozone Monitoring Instrument," *IEEE Trans. Geosci. Remote Sens.* **44** 1093–1101 (2006).
11. G. H. J. van den Oord, N. C. Rozemeijer, V. Schenkelaars, P. F. Levelt, M. R. Dobber, R. H. M. Voors, J. Class, J. de Vries, M. terLinden, C. DeHaan, and T. van de Berg, "OMI level 0 to 1B processing and operational aspects," *IEEE Trans. Geosci. Remote Sens.* **44**, 1380–1397 (2006).
12. R. Dirksen, M. Dobber, P. Levelt, G. H. J. van den Oord, G. Jaross, M. Kowalewski, G. H. Mount, D. Heath, E. Hilsenrath, and J. de Vries, "The on-ground calibration of the Ozone Monitoring Instrument from a scientific point of view," in *Proc. SPIE* **5234**, 400–410 (2003).
13. M. Dobber, R. Dirksen, P. F. Levelt, G. H. J. van den Oord, G. Jaross, M. Kowalewski, G. H. Mount, D. Heath, E. Hilsenrath,

- and R. Cebula, "Ozone Monitoring Instrument flight-model on-ground and in-flight calibration," in *International Conference on Space Optics (ICSO), Toulouse, France, 30 March–2 April 2004*, European Space Agency (ESA) publication SP-554, (ESA, 2004).
14. J. de Vries, G. H. J. van den Oord, E. Hilsenrath, M. te Plate, P. Levelt, and R. Dirksen, "Ozone Monitoring Instrument (OMI)," in Proc. SPIE **4480**, 315–325 (2001).
 15. E. Laan, D. de Winter, J. de Vries, P. Levelt, G. H. J. van den Oord, A. Maelkki, G. Leppelmeier, and E. Hilsenrath, "Towards the use of the Ozone Monitoring Instrument (OMI)," in Proc. SPIE **4540**, 193–201 (2001).
 16. K. Smorenburg, M. Dobber, E. Schenkeveld, R. Vink, and H. Visser, "Slit function measurement optical stimulus," in Proc. SPIE **4881**, 511–520 (2002).
 17. R. L. Kurucz, I. Furenlid, J. Brault, and L. Testerman, *Solar Flux Atlas from 296 to 1300 nm* (National Solar Observatory, Sunspot, N. Mex., 1984).